Monthly Notices
of the
ROYAL ASTRONOMICAL SOCIETY

Mon. Not. R. Astron. Soc. **425,** 2069–2082 (2012) doi:10.1111/j.1365-2966.2012.21196.x

X-ray, lensing and Sunyaev–Zel'dovich triaxial analysis of Abell 1835 out to R_{200}

Andrea Morandi,[1⋆] Marceau Limousin,[2,3] Jack Sayers,[4] Sunil R. Golwala,[4] Nicole G. Czakon,[4] Elena Pierpaoli,[5] Eric Jullo,[2,6] Johan Richard[3,7] and Silvia Ameglio[5]

[1]*Raymond and Beverly Sackler School of Physics and Astronomy, Tel Aviv University, Tel Aviv 69978, Israel*
[2]*Laboratoire d'Astrophysique de Marseille, Université de Provence, CNRS, 38 rue Frédéric Joliot-Curie, F-13388 Marseille Cedex 13, France*
[3]*Dark Cosmology Centre, Niels Bohr Institute, University of Copenhagen, Juliane Maries Vej 30, DK-2100 Copenhagen, Denmark*
[4]*Division of Physics, Mathematics, and Astronomy, California Institute of Technology, Pasadena, CA 91125, USA*
[5]*University of Southern California, Los Angeles, CA 90089, USA*
[6]*Propulsion Laboratory, California Institute of Technology, Pasadena, CA 91109, USA*
[7]*CRAL, Observatoire de Lyon, Université Lyon 1, 9 Avenue Ch. André, 69561 Saint Genis Laval Cedex, France*

Accepted 2012 April 26. Received 2012 April 21; in original form 2011 November 24

ABSTRACT

The measurement of the intrinsic shape and orientation of dark matter (DM) and intracluster (IC) gas in galaxy clusters is crucial for constraining their formation and evolution, and for enhancing the use of clusters as more precise cosmological probes. Extending our previous works, for the first time we present the results from a triaxial joint analysis of the galaxy cluster Abell 1835, using X-ray, strong lensing (SL) and Sunyaev–Zel'dovich (SZ) data. We parametrically reconstruct the full three-dimensional structure (triaxial shape and principal axis orientation) of both the DM and the IC gas, and the level of non-thermal pressure of the IC gas. We find that the intermediate–major and minor–major axial ratios of the DM are 0.71 ± 0.08 and 0.59 ± 0.05, respectively, and that the major axis of the DM halo is inclined with respect to the line of sight at 18.3 ± 5.2 deg. We present the first observational measurement of the non-thermal pressure out to R_{200}. This has been evaluated to be a few per cent of the total energy budget in the internal regions, while it reaches approximately 20 per cent in the outer volumes. We discuss the implications of our method for the viability of the cold dark matter (CDM) scenario, focusing on the concentration parameter C and the inner slope of the DM γ in order to test the CDM paradigm for structure formation. We measure $\gamma = 1.01 \pm 0.06$ and $C = 4.32 \pm 0.44$; these values are close to the predictions of the CDM model. The combination of X-ray/SL data at high spatial resolution, which are capable of resolving the cluster core, with the SZ data, which are more sensitive to the cluster outer volume, allows us to characterize the level and the gradient of the gas entropy distribution and non-thermal pressure out to R_{200}. Thus, we break the degeneracy among the physical models describing the thermal history of the intracluster medium.

Key words: gravitational lensing: strong – galaxies: clusters: general – galaxies: clusters: individual: Abell 1835 – cosmic background radiation – cosmology: observations – X-rays: galaxies: clusters.

1 INTRODUCTION

With the use of the cold dark matter (CDM) paradigm, there has been remarkable success in predicting the large-scale distribution of matter in the Universe, as well as its observed evolution from the earliest epochs to the present day. A fundamental prediction of N-body simulations is that CDM haloes follow a self-similar density profile, with the logarithmic slope of the dark matter (DM) γ following a shallow power law at small radii ($\gamma \sim 1$), which then steepens at larger radii (Navarro, Frenk & White 1996). However, there is still no comprehensive physical explanation for the origin of such a profile. Moreover, in recent years, there has been much interest in possible discrepancies that remain for the observed and predicted inner density profiles of structures (Limousin et al. 2008; Sand et al. 2008; Newman et al. 2011).

⋆E-mail: andrea@wise.tau.ac.il

In this perspective, clusters are the optimal place to test the predictions of cosmological simulations regarding the mass profile of dark haloes, and to cast light, in general, on the viability of the standard cosmological framework, which consists of a cosmological constant and cold dark matter (ΛCDM) with Gaussian initial conditions, by comparing the measured and predicted physical parameters (e.g. the concentration parameter, the inner slope of DM). For example, observations based on a combination of strong lensing (SL) and stellar kinematics have yielded flat inner slopes ($\gamma \simeq 0.5$) for two well-studied clusters (MS2137-23 and Abell 383; Sand et al. 2008). Also, Newman et al. (2011) have derived a shallow cusp with $\gamma < 0.3$ (68 per cent) for Abell 611, raising doubts about the predictions of the CDM scenario. Other studies have led to large scatter in the value of γ from one cluster to another, but these determinations customarily rely on the standard spherical modelling of galaxy clusters. The possible elongation/flattening of the sources along the line of sight, as well as the degeneracy of γ with other parameters (i.e. the concentration parameter and the scale radius) are likely to affect the estimated values of γ (Morandi, Pedersen & Limousin 2010).

We can also use clusters as an optimal tool to constrain the cosmological parameters, provided that we can accurately determine their mass. For example, a comparison of the cluster baryon fraction $f_{\rm b}$ with the cosmic baryon fraction can provide a direct constraint on the mean mass density of the Universe, $\Omega_{\rm m}$ (Ettori et al. 2009), while the evolution of the cluster mass function can tightly constrain Ω_Λ and the dark energy equation of state parameter w (Mantz et al. 2010). Cluster mass profiles can be probed using several independent techniques, which rely on different physical mechanisms and require different assumptions.

So far, the analyses of the cluster X-ray/Sunyaev–Zel'dovich (SZ) emission and of the gravitational lensing effect have been among the most promising techniques with which to estimate galaxy cluster masses. Concerning the former, the cluster mass can be measured by studying the intracluster (IC) gas emission under the assumption of hydrostatic equilibrium (HE; see Sarazin 1988). Indeed, the IC gas emits via both thermal bremsstrahlung in the X-ray band and inverse Compton with the photons of the cosmic microwave background (CMB) spectrum, a process known as the SZ effect (Sunyaev & Zel'dovich 1970). The X-ray mass estimate is less biased compared with the SZ and lensing-derived masses with regard to projection effects, because the emission is traced by the square of the gas density.

The advantage of the SZ effect compared with X-ray emission is the possibility of exploring clusters at higher redshift, because of the absence of cosmological dimming. Moreover, because the SZ intensity depends linearly on the density, unlike the density-squared dependence of the X-ray flux, with the SZ effect it is possible to study clusters without the systematic errors caused by the presence of subclumps and gas in the multiphase state. Also, we can study the physics of the intracluster medium (ICM) well beyond the regions constrained by X-ray observations ($\leq$0.3–0.5 R_{200}).

On the other hand, the gravitational lensing effect allows for the determination of the projected surface mass density of the lens, regardless of its dynamical state and independent of the assumption of HE (Miralda-Escude & Babul 1995). Unfortunately, in most cosmological applications, the projected mass is not the interesting quantity. Rather, we need to measure the three-dimensional mass profile, customarily by assuming spherical symmetry. Lensing mass measurements are also appreciably prone to contamination from foreground and background sources.

Knowledge of the intrinsic shape and orientation of haloes is crucial in order to obtain unbiased determinations of their masses, the inner slope of the DM and the concentration parameter via, for example, X-ray, SZ and lensing data. From this perspective, clusters are commonly modelled as spherical systems whose IC gas is in strict HE (i.e. the equilibrium gas pressure is provided entirely by thermal pressure). These assumptions are only rough approximations, leading to large biases in the determination of the cluster mass and hence on the desired cosmological parameters. Indeed, N-body simulations indicate that DM haloes are triaxial with intermediate-major and minor-intermediate axial ratios, typically of the order of $\sim$0.8 (Shaw et al. 2006; Wang & White 2009). Moreover, hydrodynamical numerical simulations suggest that the plasma in apparently relaxed systems might also be affected by additional non-equilibrium processes, which serve to boost the total pressure, and therefore cause an underestimate of the cluster mass from X-ray/SZ observations (Ameglio et al. 2009; Lau, Kravtsov & Nagai 2009; Meneghetti et al. 2010a).

On the observational side, only a few authors have tried to infer the shape or orientation of single objects (Oguri et al. 2005; Corless, King & Clowe 2009; Mahdavi & Chang 2011; Morandi & Limousin 2012), and the non-thermal pressure support (Mahdavi et al. 2008; Sanders, Fabian & Smith 2011; Richard et al. 2010; Morandi & Limousin 2012). Using a joint X-ray and lensing analysis, Morandi et al. (2010, 2011b), Morandi, Pedersen & Limousin (2011a) and Morandi & Limousin (2012) overcame the limitations of the standard spherical modelling and strict HE assumption, in order to infer the desired three-dimensional shape and physical properties of galaxy clusters in a bias-free way. A triaxial joint analysis relying on independent and multifrequency data sets for galaxy clusters can relax the assumptions customarily adopted in the cluster analysis, and it can give us additional insights into the underlying physics of these objects.

Extending the findings of our previous works, in this paper we recover the full triaxiality of both the DM and the ICM (i.e. ellipsoidal shape and principal axis orientation) and the level and the gradient of non-thermal pressure for the galaxy cluster Abell 1835. This cluster is a luminous cool-core galaxy cluster at $z = 0.253$ and it is an optimal candidate for a triaxial joint analysis using X-ray, SZ and lensing techniques, because of its very relaxed dynamical appearance and its exceptional SL system. We discuss the implications of our findings for the viability of the CDM scenario, focusing on the concentration parameter and the inner slope of the DM.

Because of the availability of SZ data out to R_{200}, we can infer the properties of the ICM in the outskirts of the galaxy cluster. An accurate measurement of the properties of galaxy clusters out to large radii can provide critical insight into the physics of the ICM and it offers a direct probe of the assembly history of structure formation on the largest scales. Also, it enhances the use of clusters as cosmological probes, because the physics of the IC gas in the outer volumes is relatively simple and nearly self-similar. In particular, we compare our findings with the results of hydrodynamical numerical simulations for the density, temperature, entropy and non-thermal pressure profiles out to the virial radius.[1]

Throughout this paper, we assume a flat ΛCDM cosmology; the matter density parameter has the value $\Omega_{\rm m} = 0.3$, the cosmological

[1] Hereafter, we equate the virial radius with R_{200}, the radius within which the mean total density is 200 times the critical density of the Universe at the redshift of the cluster.

constant density parameter is $\Omega_\Lambda = 0.7$ and the Hubble constant is $H_0 = 70$ km s^{-1} Mpc^{-1}. At the cluster redshift and for the assumed cosmological parameters, 1 arcsec is equivalent to 3.9 kpc. Unless otherwise stated, quoted errors are at the 68.3 per cent confidence level.

2 STRONG LENSING MODELLING

In a forthcoming publication, we will present a detailed mass model of Abell 1835 and a description of the data used. We summarize it in this section.

2.1 Multiple images

The last SL model of Abell 1835 was presented by Richard et al. (2010).

Since then, Abell 1835 has been observed with the Wide Field Camera 3 (WFC3) onboard the *Hubble Space Telescope* (*HST*) in the F110W and F160W filters (programme 10591; PI, Kneib). These new imaging data have allowed the identification of new multiply imaged systems in the cluster core. Moreover, a spectroscopic campaign that targeted multiple images was carried out using the focal reducer/low dispersion spectrograph 2 (FORS2) on the Very Large Telescope (VLT; programme 087.A-0326; PI, Jullo). This yielded a spectroscopic measurement for some multiple images.

The model presented by Richard et al. (2010) was based on seven multiply imaged systems, two of which have a measured spectroscopic redshift. In this paper, the model is based on eight multiply imaged systems, six of which are spectroscopically confirmed. For the remaining systems, the redshifts are allowed to be free during the optimization. These images are listed in Table 1 and they are shown in Fig. 1.

Table 1. The multiply imaged systems considered in this paper. Redshift measurement and estimation will be presented in a forthcoming publication.

ID	RA	Dec.
1.1	210.26573	2.8706065
1.2	210.26403	2.869229
1.3	210.24724	2.8699809
2.1	210.26613	2.8741627
2.2	210.26372	2.8714114
2.3	210.24826	2.8717531
3.1	210.26325	2.8850109
3.2	210.26276	2.885247
3.3	210.24374	2.8775381
4.1	210.26381	2.8847053
4.2	210.26072	2.885872
4.3	210.24434	2.8781354
5.1	210.25984	2.8824075
5.2	210.24484	2.8721518
5.3	210.25921	2.8792670
6.1	210.25635	2.8680176
6.2	210.25283	2.8688838
6.3	210.26841	2.8732770
7.1	210.25379	2.8732994
7.2	210.25420	2.8803349
7.3	210.27108	2.8801023
7.4	210.25417	2.8730285
8.1	210.26094	2.8821034
8.2	210.24495	2.8731514
8.3	210.25958	2.8790901

2.2 Mass distribution

The model of the cluster mass distribution comprises three mass components, described using a dual pseudo-isothermal elliptical mass distribution (dPIE; Limousin, Kneib & Natarajan 2005; Elíasdóttir et al. 2007), parametrized by a fiducial velocity dispersion σ, a core radius $r_{\rm core}$ and a scale radius $r_{\rm s}$: (i) a cluster-scale DM halo; (ii) the stellar mass in the brightest cluster galaxy (BCG); (iii) the cluster galaxies representing local perturbation. As in earlier works (e.g. Limousin et al. 2007a), empirical relations (without any scatter) are used to relate their dynamical dPIE parameters (central velocity dispersion and scale radius) to their luminosity (the core radius being set to a vanishing value, 0.05 kpc), whereas all geometrical parameters (centre, ellipticity and position angle) are set to the values measured from the light distribution. Because they are close to multiple images, following Richard et al. (2010), two cluster galaxies are modelled individually, namely P1 and P2 (Fig. 1). Their scale radii and velocity dispersions are optimized individually. We allow the velocity dispersion of the cluster galaxies to vary between 100 and 250 km s^{-1}, whereas the scale radius is forced to be less than 70 kpc in order to account for the tidal stripping of their DM haloes (e.g. Limousin et al. 2007b, 2009; Natarajan et al. 2009; Wetzel & White 2010, and references therein).

Concerning the cluster-scale DM halo, we set its scale radius to 1000 kpc because we do not have data to constrain this parameter.

The optimization is performed in the image plane, using the LENSTOOL[2] software (Jullo et al. 2007).

2.3 Strong lensing results

The rms in the image plane is equal to 1.4 arcsec. In good agreement with Richard et al. (2010), we find that Abell 1835 is well described by a unimodal mass distribution. We note that the galaxy-scale perturbers all present a scale radius that is smaller than the scale radius inferred for isolated field galaxies, in agreement with the tidal stripping scenario.

The LENSTOOL software does explore the parameter space using a Monte Carlo Markov chain (MCMC) sampler. At the end of the optimization, we have access to these MCMC realizations from which we can draw statistics and estimate error bars. For each realization, we build a two-dimensional mass map. All these mass maps are then used to compute the mean mass map and the corresponding covariance matrix. Note that we have checked that the probability distribution function (PDF) of the mass in each pixel is approximately Gaussian. This information is then used in the joint fit.

3 X-RAY DATA SETS AND ANALYSIS

The cluster Abell 1835 is a luminous cluster at redshift $z = 0.253$, which exhibits several indications of a well-relaxed dynamical state; for instance, its X-ray emission peak is associated with a cool core

[2] http://www.oamp.fr/cosmology/lenstool/

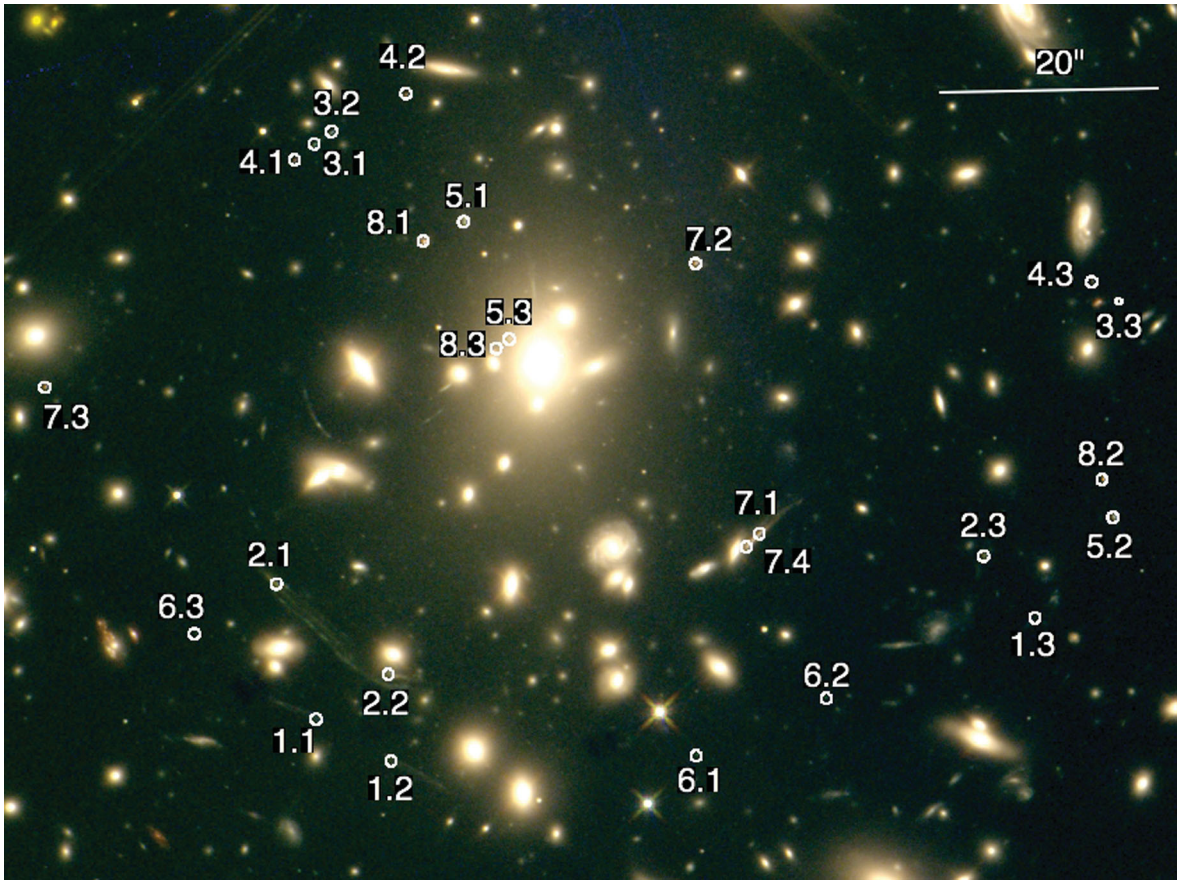

Figure 1. Core of Abell 1835. The size of the field equals 82×82 arcsec^2, corresponding to 286×286 kpc^2. The multiply imaged systems used in this paper are labelled.

and it is well centred on the BCG. The X-ray isophotes appear to be regular, with a low degree of ellipticity, and with the absence of evident substructures. The global (cooling-core corrected) temperature $T_{\rm ew}$ has been estimated to be $T_{\rm ew} = 9.38 \pm 0.11$ keV and the abundance has been evaluated in 0.48 ± 0.03 solar value (Section 3.1). We classify this cluster as a strong cooling-core source (SCC; Morandi & Ettori 2007); that is, the central cooling time $t_{\rm cool}$ is less than the age of the Universe $t_{{\rm age},z}$ at the cluster redshift ($t_{\rm cool}/t_{{\rm age},z} < 0.1$). We have estimated $t_{\rm cool} \simeq 1 \times 10^9$ yr. As with other SCCs, Abell 1835 shows a low central temperature ($\sim$5 keV) and a strong spike of luminosity in the brightness profile. The temperature profile is very regular, as expected for relaxed clusters (see the upper panel of Fig. 2).

A full description of the X-ray analysis can be found in Morandi & Limousin (2012). Here, we only briefly summarize the most relevant or novel aspects of our data reduction and analysis of Abell 1835.

3.1 X-ray data reduction

We have reduced the *Chandra* X-ray data using the CIAO data analysis package, version 4.3, and the calibration data base CALDB 4.4.3. Here, we briefly summarize the reduction procedure. We have performed our X-ray analysis on four data sets retrieved from the National Aeronautics and Space Administration (NASA) HEASARC archive (observation IDs 6880, 6881, 7370 and 496) with a total exposure time of approximately 200 ks. Three observations (IDs 6880, 6881 and 7370) have been carried out using the Advanced CCD Imaging Spectrometer I-array (ACIS-I) and telemetered in the very faint mode and one observation (ID 496) has been carried out using the ACIS-S and telemetered in the faint mode (ID 2321). The level-1 event files were reprocessed to apply the appropriate gain maps and calibration products and to reduce the ACIS quiescent background. We used the `acis_process_events` tool to check for cosmic ray background events and to correct for eventual spatial gain variations caused by charge transfer inefficiency in order to recompute the event grades. Then, we filtered the data to include the standard events grades 0, 2, 3, 4 and 6 only, and therefore we have filtered for the good time intervals (GTIs) supplied, which are contained in the `flt1.fits` file. The bright point sources were identified and masked out using the script `vtpdetect`, and the result was then checked by visual inspection.

Then we used the tool `dmextract` to create the light curve of the background. Indeed, a careful screening of the background light curve is necessary for a correct background subtraction and to discard contaminating flare events. In order to clean the data sets of periods of anomalous background rates, we used the `deflare` script, so as to filter out the times where the background count rate exceeds $\pm 3\sigma$ of the mean value. Finally, we filtered the ACIS event files on energy, by selecting the range 0.3–12 keV, and on CCDs, so as to obtain a level-2 event file.

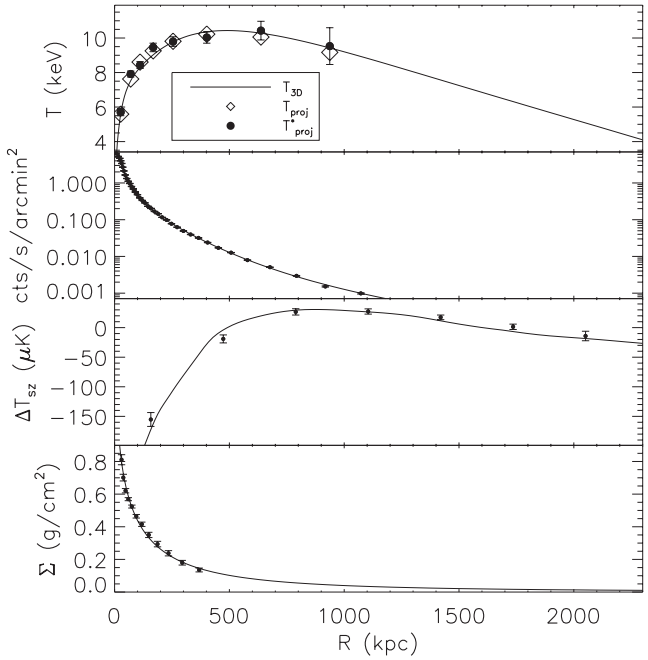

Figure 2. Example of the joint analysis of T, S_X, $\Delta T_{SZ}(\nu)$ and Σ. In the upper panel, we display the two quantities from the X-ray analysis (equation 14): the observed spectral projected temperature $T^*_{\mathrm{proj},m}$ (large dots with error bars) and the theoretical projected temperature $T_{\mathrm{proj},m}$ (diamonds). We also show the theoretical three-dimensional temperature (solid line), which generates $T_{\mathrm{proj},m}$ through convenient projection techniques. In the second panel from the top, we display the two quantities from the X-ray brightness analysis (equation 15): the observed and theoretical surface brightness profiles S^*_X (points with error bars) and S_X (solid line), respectively. In the third panel from the top, we display the two quantities from the SZ temperature decrement analysis (equation 9): the observed SZ temperature decrement profile (points with error bars) and the theoretical one $\Delta T_{SZ}(\nu)$ (solid line). Both the observed and theoretical SZ temperature decrements are convolved with the transfer function. Note that this filtering significantly reduces the peak decrement of the cluster and creates a ring of positive flux at $r \sim 2$ arcmin. In the lowest panel, we display the two quantities from the lensing analysis (equation 17): the observed and theoretical surface mass profiles Σ^* (points with error bars) and Σ (solid line), respectively. Note that for the surface brightness (surface mass) and SZ data, the one-dimensional profile has been presented only for visualization purposes, with the fit applied to the two-dimensional data. Moreover, for the surface brightness, we have plotted data referring to the observation ID 6880. The virial radius corresponds to a scalelength on the plane of the sky of $\sim\eta_{\mathrm{DM,a}}R_{200} \approx 2240$ kpc.

3.2 X-ray spatial and spectral analysis

We measure the gas density profile from the surface brightness recovered by a spatial analysis, and we infer the projected temperature profile by analysing the spectral data.

The X-ray images were extracted from the level-2 event files in the energy range (0.5–5.0 keV), corrected by the exposure map to remove the vignetting effects. Point sources were then masked and the images were rebinned by a factor of 4 (1 pixel = 1.968 arcsec).

We determined the centroid (x_c, y_c) of the surface brightness by locating the position where the X and Y derivatives go to zero, which is usually a robust and outlier-resistance approach. We have checked that the X-ray emission is centred on the BCG; the distance between the X-ray centroid and the BCG centre is $\simeq$1.8 arcsec (the uncertainty on this measure is comparable to the smoothing scale applied to the X-ray image to determine the centroid).

The spectral analysis was performed by extracting the source spectra in circular annuli of radius r^*_m around the X-ray surface brightness centroid. We have selected $n^* = 8$ annuli out to a maximum distance $R_{\mathrm{spec}} = 1095$ kpc, according to the following criteria. The number of net counts of photons from the source in the band used for the spectral analysis is at least 2000 per annulus, which corresponds to a fraction of the total counts always larger than 30 per cent. We used the CIAO `specextract` tool to extract the source and background spectra and to construct the redistribution matrix files (RMFs) and the ancillary response files (ARFs).

Each of the n^* annuli have been analysed using the XSPEC package (Arnaud 1996) by simultaneously fitting an absorbed optically thin plasma emission model (the MEKAL model; Kaastra 1992; Liedahl, Osterheld & Goldstein 1995) to the four observations. The fit is performed in the energy range 0.6–7 keV by fixing the redshift at $z = 0.253$, and the photoelectric absorption at the galactic value (i.e. to the value inferred from radio H I maps). For each of the n^* annuli, we grouped the photons into bins of 20 counts per energy channel and we applied χ^2-statistics. Thus, for each of the annuli, the free parameters in the spectral analysis were the normalization of the thermal spectrum $K_i \propto \int n_e^2\,\mathrm{d}V$, the emission-weighted temperature $T^*_{\mathrm{proj},i}$, and the metallicity Z_i.

The four observations were first analysed individually, to assess the consistency of the data sets and to exclude any systematic effects that could influence the combined analysis. Then, we proceeded with the joint spectral analysis of the four data sets.

The background spectra have been extracted from regions of the same exposure for the ACIS-I observations, for which we always have some areas free from source emission. We have also checked for systematic errors resulting from possible source contamination of the background regions. Conversely, for the ACIS-S observation, we have considered the ACIS-S3 chip only and we used the ACIS blank-sky background files. We have extracted the blank-sky spectra from the blank-field background data sets provided by the ACIS calibration team in the same chip regions as the observed cluster spectra. The blank-sky observations underwent a reduction procedure comparable to the one applied to the cluster data, after being reprojected on to the sky according to the observation aspect information by using the `reproject_events` tool. Then, we scaled the blank-sky spectrum level to the corresponding observational spectrum in the 9–12 keV interval, because in this band the *Chandra* effective area is negligible and thus very little cluster emission is expected. One of the advantages of this method is that the derived ARFs and RMFs will be consistent for both the source and the background spectrum. However, the background in the X-ray soft band can vary in both time and space, so it is important to check whether the background derived by the blank-sky data sets is consistent with the real one. From this perspective, we have verified that for the ACIS-I observations the two methods of background subtraction provide very similar results for the fit parameters (e.g. the temperature).

4 SZ DATA SET AND ANALYSIS

The SZ data were collected using Bolocam in 2006, and they have been presented previously in Sayers et al. (2011). Since that publication, these data have been reduced again using a slightly modified reduction pipeline, which we briefly describe here. First, the flux calibration model has been updated, based on recent *Wilkinson Microwave Anisotropy Probe* (*WMAP*) results, as described in

Sayers, Czakon & Golwala (2012). This results in <5 per cent changes to the flux calibration. Secondly, there have been some minor changes to the data-flagging procedures, which, in general, have a very small effect on the final SZ image. Thirdly, we note that the coordinates in the Abell 1835 image thumbnails in Sayers et al. (2011) are offset in declination by 1 arcmin 9 arcsec because of a typographical error in the source coordinate file for that cluster. There is no such coordinate offset for any of the other clusters presented in Sayers et al. (2011).

Although the full data reduction procedure is described in detail in Sayers et al. (2011), we briefly discuss the relevant aspects of this processing here. In particular, the data are effectively high-pass filtered in a complicated and slightly non-linear way in order to subtract noise resulting from fluctuations in the opacity of the atmosphere (i.e. the transfer function of the filtering depends weakly on the cluster profile). We fit an elliptical generalized Navarro–Frenk–White (gNFW) profile (Nagai, Kravtsov & Vikhlinin 2007; Arnaud et al. 2010) to Abell 1835, which has provided a good fit to the data (χ^2/d.o.f. = 964/945). Note that this is slightly different from the value given in table 2 of Sayers et al. (2011) (χ^2/d.o.f. = 966/945), because of the slightly different data flagging used in this analysis. The transfer function computed for this model is then used for all of our subsequent analyses (i.e. all models have been filtered using this transfer function prior to comparing them to the SZ data). We have verified that the biases associated with using this single transfer function are negligible compared to the noise in the image. The effects of this transfer function can be clearly seen in the third panel from the top of Fig. 2, where a radial profile of the SZ data is plotted.

5 THREE-DIMENSIONAL STRUCTURE OF GALAXY CLUSTERS

The lensing and the X-ray/SZ emission both depend on the properties of the DM gravitational potential well. The former is a direct probe of the two-dimensional mass map via the lensing equation and the latter is an indirect proxy of the three-dimensional mass profile through the HE equation applied to the gas temperature and density. In order to infer the model parameters of both the IC gas and of the underlying DM density profile, we perform a joint analysis of SL and X-ray/SZ data. We briefly outline the methodology in order to infer physical properties in triaxial galaxy clusters.

(i) We start with a gNFW triaxial model of the DM, as described in Jing & Suto (2002), which is representative of the total underlying mass distribution. This depends on a few parameters to be determined: the concentration parameter C; the scale radius $R_{\rm s}$; the inner slope of the DM γ; the two axial ratios ($\eta_{\rm DM,a}$ and $\eta_{\rm DM,b}$); the Euler angles ψ, θ and ϕ.

(ii) Following Lee & Suto (2003, 2004), we recover the gravitational potential and two-dimensional surface mass Σ (equation 11) of a DM halo using this triaxial density profile.

(iii) We solve the generalized HE equation (i.e. including the non-thermal pressure $P_{\rm nt}$; see equation 5) for the density of the IC gas sitting in the gravitational potential well previously calculated, in order to infer the theoretical three-dimensional temperature profile T.

(iv) We calculate the SZ temperature decrement map $\Delta T_{\rm SZ}(\nu)$ (equation 9) and the surface brightness map $S_{\rm X}$ (equation 8) related to the triaxial ICM halo.

(v) The joint comparison of T with the observed temperature, of $S_{\rm X}$ with the observed brightness image, of $\Delta T_{\rm SZ}(\nu)$ with the observed SZ temperature decrement, and of Σ with the observed two-dimensional mass map give us the parameters of the triaxial ICM and DM density models.

Here, we briefly summarize the major findings of Morandi & Limousin (2012) for the triaxial joint analysis, in order to infer the desired physical properties, as well as the improvements added in the current analysis. Additional details can be found in Morandi, Ettori & Moscardini (2007), Morandi et al. (2010, 2011a,b) and Morandi & Limousin (2012).

In Morandi & Limousin (2012), we modelled the DM and ICM ellipsoids to be orientated in a arbitrary direction on the sky. We introduced two Cartesian coordinate systems, $x = (x, y, z)$ and $x' = (x', y', z')$, which represent respectively the principal coordinate system of the triaxial dark halo and the observer's coordinate system, with the origins set at the centre of the halo. We assumed that the z'-axis lies along the line of sight to the observer and that the x', y' axes identify the directions of west and north, respectively, on the plane of the sky. We also assumed that the x, y, z-axes lie along the minor, intermediate and major axes, respectively, of the DM halo. If we define ψ, θ and ϕ as the rotation angles about the x, y and z axes, respectively, then the relation between the two coordinate systems can be expressed in terms of the rotation matrices $M_x(\psi)$, $M_y(\theta)$, $M_z(\phi)$ with Euler angles ψ, θ, ϕ:

$$x' = M_x(\psi)\#M_y(\theta)\#M_z(\phi)\#x. \tag{1}$$

In order to parametrize the cluster mass distribution, we consider a triaxial gNFW model (Jing & Suto 2002):

$$\rho(R) = \frac{\delta_{\rm c}\rho_{\rm c,z}}{(R/R_{\rm s})^{\gamma}\,(1 + R/R_{\rm s})^{3-\gamma}}. \tag{2}$$

Here, $R_{\rm s}$ is the scale radius, $\delta_{\rm c}$ is the dimensionless characteristic density contrast with respect to the critical density of the Universe $\rho_{\rm c,z}$, at the redshift z of the cluster, and γ represents the inner slope of the density profile. $\rho_{\rm c,z} \equiv 3H(z)^2/8\pi G$ is the critical density of the Universe at redshift z, $H_z \equiv E_z, H_0, E_z = [\Omega_M(1+z)^3 + \Omega_\Lambda]^{1/2}$, and

$$\delta_{\rm c} = \frac{200}{3}\frac{C^3}{F(C,\gamma)}, \tag{3}$$

where $C \equiv R_{200}/R_{\rm s}$ is the concentration parameter. $F(C, \gamma)$ has already been defined in Wyithe, Turner & Spergel (2001).

The radius R can be regarded as the major-axis length of the iso-density surfaces:

$$R^2 = c^2\left(\frac{x^2}{a^2} + \frac{y^2}{b^2} + \frac{z^2}{c^2}\right), \qquad (a \le b \le c). \tag{4}$$

We also define $\eta_{\rm DM,a} = a/c$ and $\eta_{\rm DM,b} = b/c$ as the minor–major and intermediate–major axial ratios of the DM halo, respectively, and $e_{\rm b}$ and $e_{\rm c}$ are the relative eccentricities (e.g. $e_{\rm b} = \sqrt{1-(b/c)^2}$).

Lee & Suto (2003) have shown that the iso-potential surfaces of the triaxial dark halo are well approximated by a sequence of concentric triaxial distributions of radius $R_{\rm icm}$ with different eccentricity ratios. $R_{\rm icm}$ has a similar definition as R (equation 4), but with IC gas eccentricities $\epsilon_{\rm b}$ and $\epsilon_{\rm c}$. Note that $\epsilon_{\rm b} = \epsilon_{\rm b}(e_{\rm b}, u, \gamma)$ and $\epsilon_{\rm c} = \epsilon_{\rm c}(e_{\rm c}, u, \gamma)$, with $u = R/R_{\rm s}$, unlike the constant $e_{\rm b}$, $e_{\rm c}$ for the adopted DM halo profile. In the whole range of u, $\epsilon_{\rm b}/e_{\rm b}$ ($\epsilon_{\rm c}/e_{\rm c}$) is less than unity ($\sim$0.7 at the centre). That is, the IC gas is altogether more spherical than the underlying DM halo (see Morandi et al. 2010 for further details).

5.1 X-ray, SZ and lensing equations

For the X-ray analysis, we rely on a generalization of the HE equation (Morandi et al. 2011b), which accounts for the non-thermal pressure $P_{\rm nt}$:

$$\nabla P_{\rm tot} = -\rho_{\rm gas} \nabla \Phi. \quad (5)$$

Here, $\rho_{\rm gas}$ is the gas mass density, Φ is the gravitational potential and $P_{\rm tot} = P_{\rm th} + P_{\rm nt}$. We have implemented a model where $P_{\rm nt}$ is a fraction of the total pressure $P_{\rm tot}$, and we set this fraction to be a power law with radius (Shaw et al. 2010):

$$\frac{P_{\rm nt}}{P_{\rm tot}} = \xi (R/R_{200})^n. \quad (6)$$

Note that X-ray and SZ data probe only the thermal component of the gas $P_{\rm th} = n_{\rm e} k_{\rm b} T$, where $k_{\rm b}$ is the Boltzmann constant. From equations (5) and (6), we can see that neglecting $P_{\rm nt}$ (i.e. $P_{\rm tot} = P_{\rm th}$) systematically bias low the determination of cluster mass profiles. We stress that the model in equation (6) is an improvement with respect to that of Morandi & Limousin (2012), where we have assumed that the non-thermal pressure is a constant fraction of the total pressure.

Given that equation (5) is a first-order differential equation, we need a boundary condition on the pressure, $\tilde{P}$, which represents the pressure at R_{200}, and this is an unknown parameter to be determined.

To model the electron density profile in the triaxial ICM halo, we use the following fitting function

$$n_{\rm e}(R_{\rm icm}) = n_0 (R_{\rm icm}/r_{c_1})^{-\delta} \left(1 + R^2_{\rm icm}/r^2_{c_1}\right)^{-3/2\,\varepsilon + \delta/2} \times \left(1 + R^4_{\rm icm}/r^4_{c_2}\right)^{-\upsilon/4}, \quad (7)$$

with parameters $(n_0, r_{c_1}, \varepsilon, \delta, r_{c_2}, \upsilon)$. Note that the fitting function in equation (7) has more degrees of freedom than that employed in Morandi & Limousin (2012). We have computed the theoretical three-dimensional temperature T by numerically integrating the equation of the HE (equation 5), assuming triaxial geometry and a functional form of the gas density given by equation (7).

The observed X-ray surface brightness $S_{\rm X}$ is given by

$$S_{\rm X} = \frac{1}{4\pi (1+z)^4} \Lambda \left(T^*_{\rm proj}, Z\right) \int n_{\rm e} n_{\rm p}\, {\rm d}z', \quad (8)$$

where $\Lambda(T^*_{\rm proj}, Z)$ is the cooling function. Because the projection on the sky of the plasma emissivity gives the X-ray surface brightness, the latter can be geometrically fitted with the model $n_{\rm e}(R_{\rm icm})$ of the assumed distribution of the electron density (equation 7) by applying equation (8). This has been accomplished by using fake *Chandra* spectra, where the current model is folded through response curves (ARFs and RMFs) and then it is added to a background file, with absorption, temperature and metallicity measured in the neighbouring ring in the spectral analysis (Section 3.2). In order to calculate $\Lambda(T^*_{\rm proj}, Z)$, we have adopted a MEKAL model (Kaastra 1992; Liedahl et al. 1995) for the emissivity.

The thermal SZ effect is expressed as a small variation in the temperature $\Delta T_{\rm SZ}(\nu)$ of the CMB as a function of the observation frequency:

$$\frac{\Delta T_{\rm SZ}(\nu)}{T_{\rm cmb}} = \frac{\sigma_{\rm T}}{m_{\rm e} c^2} \int P_{\rm e}(r) f[\nu; T(r)]\, {\rm d}z'. \quad (9)$$

Here, $\sigma_{\rm T}$ is the Thomson cross-section, $P_{\rm e}(r) \equiv n_{\rm e}(r) k_b T(r)$ is the pressure of the electrons of the ICM at the volume element of coordinate r, $k_{\rm b}$ is the Boltzmann constant and $T_{\rm cmb} = 2.725$ K.

$f[\nu; T(r)]$ takes into account the spectral shape of the SZ effect, as follows

$$f[\nu; T(r)] = \left(x \frac{e^x + 1}{e^x - 1} - 4\right) \left[1 + o_f(x; T)\right]. \quad (10)$$

Here, $x = h\nu/kT_{\rm cmb}$ accounts for the frequency dependence of the SZ effect, and for the relativistic corrections related to the term $o_f(x, T)$ (Itoh, Kohyama & Nozawa 1998). Note that, in equation (9), we account for the implicit dependence of $f[\nu; T(r)]$ on radius.

Next, the two-dimensional SZ model $\Delta T_{\rm SZ}(\nu)$ is convolved with the Bolocam point spread function and the measured transfer function. In practice, the transfer function convolution is performed by multiplication in the Fourier domain. This filtering significantly reduces the peak decrement of the cluster and it creates a ring of positive flux at $r \sim 2$ arcmin. This filtered model is then compared to the observed SZ temperature decrement map. We have also calculated the noise covariance matrix $\mathbf{C}$ among all the pixels of the observed SZ temperature decrement map through 1000 jack-knife realizations of our cluster noise. In this perspective, we have assumed that the noise covariance matrix for the SZ data is diagonal, because this was shown to be a good assumption in Sayers et al. (2011).

For the lensing analysis, the two-dimensional surface mass density Σ can be expressed as

$$\Sigma = \int_{-\infty}^{\infty} \rho(R)\, {\rm d}z'. \quad (11)$$

We have also calculated the covariance matrix $\mathbf{C}$ among all the pixels of the reconstructed surface mass (see Morandi et al. 2011b, for further details).

5.2 Joint X-ray+SZ+lensing analysis

The PDF of the model parameters has been evaluated with an MCMC algorithm, by using the likelihood $\mathcal{L}$ described below as a proposal density and a standard method for rejecting proposed moves. This allows us to compare observations and predictions, and to infer the desired physical parameters. The likelihood has been constructed by performing a joint analysis for SL and X-ray/SZ data. More specifically, the system of equations that we simultaneously rely on in our joint X-ray+SZ+lensing analysis is

$$T(C, R_{\rm s}, \gamma, \eta_{\rm DM,a}, \eta_{\rm DM,b}, \psi, \theta, \phi, n_0, r_{c_1}, \varepsilon, \delta, r_{c_2}, \upsilon, \xi, n, \tilde{P})$$

$$S_{\rm X}(C, R_{\rm s}, \gamma, \eta_{\rm DM,a}, \eta_{\rm DM,b}, \psi, \theta, \phi, n_0, r_{c_1}, \varepsilon, \delta, r_{c_2}, \upsilon)$$

$$\Delta T_{\rm SZ}(C, R_{\rm s}, \gamma, \eta_{\rm DM,a}, \eta_{\rm DM,b}, \psi, \theta, \phi, n_0, r_{c_1}, \varepsilon, \delta, r_{c_2}, \upsilon, \xi, n, \tilde{P})$$

$$\Sigma(C, R_{\rm s}, \gamma, \eta_{\rm DM,a}, \eta_{\rm DM,b}, \psi, \theta, \phi). \quad (12)$$

Here, the parameters C (concentration parameter), $R_{\rm s}$ (scale radius), γ (inner DM slope), $\eta_{\rm DM,a}$ (minor–major axial ratio), $\eta_{\rm DM,b}$ (intermediate–major axial ratio) and ψ, θ, ϕ (Euler angles) refer to the triaxial DM halo (equation 2). The parameters n_0, r_{c_1}, ε, δ, r_{c_2} and υ refer to the IC gas density (equation 7), ξ and n (normalization and slope, respectively) refer to the non-thermal pressure (equation 6) and $\tilde{P}$ refers to the pressure at R_{200}, which is a boundary condition of the generalized HE equation (equation 5).

In our triaxial joint analysis, the three-dimensional model temperature T is recovered by solving equation (5) and it is constrained by the observed temperature profile. The surface brightness is recovered via projection of the gas density model (equation 8) and it is constrained by the observed brightness. The SZ signal is deduced using the projection of the three-dimensional pressure (equation 9) and it is constrained by the observed SZ temperature decrement. The model two-dimensional mass Σ is recovered by using equation (11) and it is constrained by the observed surface mass.

Hence, the likelihood $\mathcal{L} \propto \exp(-\chi^2/2)$, and χ^2 is

$$\chi^2 = \chi^2_{\mathrm{x},T} + \chi^2_{\mathrm{x},S} + \chi^2_{\mathrm{SZ}} + \chi^2_{\mathrm{lens}}, \quad (13)$$

where $\chi^2_{\mathrm{x},T}$, $\chi^2_{\mathrm{x},S}$, χ^2_{SZ} and χ^2_{lens} denote χ^2 coming from the X-ray temperature, X-ray brightness, SZ temperature decrement and lensing data, respectively.

For the spectral analysis, $\chi^2_{\mathrm{x},T}$ is equal to

$$\chi^2_{\mathrm{x},T} = \sum_{i=1}^{n^*} \frac{\left(T_{\mathrm{proj},i} - T^*_{\mathrm{proj},i}\right)^2}{\sigma^2_{T^*_{\mathrm{proj},i}}}, \quad (14)$$

where $T^*_{\mathrm{proj},i}$ is the observed projected temperature profile in the ith circular ring and $T_{\mathrm{proj},i}$ is the azimuthally averaged projection (following Mazzotta et al. 2004) of the theoretical three-dimensional temperature T; the latter is the result of solving the HE equation, with the gas density $n_{\mathrm{e}}(R_{\mathrm{icm}})$.

For the X-ray brightness, $\chi^2_{\mathrm{x,S}}$ is

$$\chi^2_{\mathrm{x},S} = \sum_j \sum_{i=1}^{N_j} \frac{(S_{\mathrm{X},i} - S^*_{\mathrm{X},i})^2}{\sigma^2_{S,i}}, \quad (15)$$

where $S_{\mathrm{X},i}$ and $S^*_{\mathrm{X},i}$ are equal to the theoretical and observed counts in the ith pixel of the jth image. Given that the number of counts in each bin might be small (<5), we cannot assume that the Poisson distribution from which the counts are sampled has a nearly Gaussian shape. The standard deviation (i.e. the square-root of the variance) for this low-count case has been derived by Gehrels (1986) as

$$\sigma_{S,i} = 1 + \sqrt{S^*_{\mathrm{X},i} + 0.75}, \quad (16)$$

which has been demonstrated to be accurate to approximately 1 per cent. Note that we have added background to $S_{\mathrm{X},i}$ as measured locally in the brightness images, and that vignetting has been removed in the observed brightness images.

For the SZ (lensing) constraint D, the χ^2_D contribution is

$$\chi^2_D = [D - D^*]^{\mathrm{t}} \mathbf{C}^{-1} [D - D^*], \quad (17)$$

where $\mathbf{C}$ is the covariance matrix of the two-dimensional SZ temperature decrement (projected mass), D^* are the observed measurements of the two-dimensional SZ temperature decrement (projected mass) in the ith pixel and D is the theoretical two-dimensional model. Note that we have removed the central 25 kpc of the two-dimensional projected mass in the joint analysis, to avoid contamination from the central dominant (cD) galaxy mass.

We report the average value and standard deviation of the marginal probability distribution for the individual parameters. In addition to a complete statistical analysis of the chain, we have performed a series of convergence tests: R statistics of Gelman & Rubin (1992) and a split-test, which essentially consists of splitting the chain into two, three or four parts and comparing the difference in the parameter quantiles. We have confirmed the convergence of our result using these tests.

Thus we can determine the physical parameters of the cluster (e.g. the three-dimensional temperature T, or the shape of the DM and the ICM) by relying on the generalized HE equation and on the robust results of the hydrodynamical simulations of the DM profiles (i.e. gNFW). We should point out that, given the complementary data sets that have been included in this analysis, we do not need to rely on any prior from theoretical predictions, such as priors on the concentration parameter, on the halo mass or on the axial ratios (e.g. Corless et al. 2009), which might be biased because of our incomplete understanding of the cluster physics in simulations.

Fig. 2 presents an example of a joint analysis for T, S_{X}, $\Delta T_{\mathrm{SZ}}(\upsilon)$ and Σ; for S_{X}, $\Delta T_{\mathrm{SZ}}(\upsilon)$ and Σ, the one-dimensional profile has been presented only for visualization purposes, with the fit applied to the two-dimensional X-ray brightness/SZ/surface mass data. Note that in the joint analysis the X-ray, SZ and lensing data are all well described by our model, with $\chi^2_{\mathrm{red}} = 1.04$ (1 477 928 degrees of freedom).

6 RESULTS AND DISCUSSION

In the previous section, we have shown how we can determine the physical parameters of the cluster by fitting the available data, relying on the HE equation and on a DM model that is based on the robust results of hydrodynamical cluster simulations. In this section, we present our results and we discuss their main implications. We particularly focus on the implications of our analysis for the determination of the full triaxiality, the viability of the CDM scenario, the presence of non-thermal pressure and the gas properties in the outskirts.

6.1 Model parameters

The model parameters are summarized in Table 2. Our work indicates that Abell 1835 is a triaxial galaxy cluster with DM halo axial ratios $\eta_{\mathrm{DM,a}} = 0.59 \pm 0.05$ and $\eta_{\mathrm{DM,b}} = 0.71 \pm 0.08$, and with the major axis slightly inclined with respect to the line of sight of $\theta = 18.3 \pm 5.2$ deg. Our findings give support to this view of a triaxial cluster elongated along the line of sight and they agree with the predictions of Oguri & Blandford (2009), who have

Table 2. Model parameters of Abell 1835. Rows 1–8 give the model parameters: C (concentration parameter), R_{s} (scale radius), γ (inner DM slope), $\eta_{\mathrm{DM,a}}$ (minor–major axial ratio), $\eta_{\mathrm{DM,b}}$ (intermediate–major axial ratio) and ψ, θ, ϕ (Euler angles) of the DM halo (equation 2). Rows 9–14 give the model parameters n_0, r_{c_1}, ε, δ, r_{c_2} and υ of the IC gas density (equation 7). Rows 15 and 16 give the model parameters ξ and n (normalization and slope, respectively) of the non-thermal pressure (equation 6). Finally, the last row gives the model parameter $\tilde{P}$ of the pressure at R_{200}, which is a boundary condition of the generalized HE equation (equation 5).

C	4.32 ± 0.44
R_{s} (kpc)	891.0 ± 114.3
γ	1.01 ± 0.06
$\eta_{\mathrm{DM,a}}$	0.59 ± 0.05
$\eta_{\mathrm{DM,b}}$	0.71 ± 0.08
ψ (deg)	-55.0 ± 6.9
θ (deg)	18.3 ± 5.2
ϕ (deg)	3.8 ± 4.6
n_0 (cm^{-3})	0.018 ± 0.002
r_{c_1} (kpc)	117.7 ± 10.1
ε	0.68 ± 0.02
δ	0.82 ± 0.03
r_{c_2} (kpc)	1674.3 ± 266.7
υ	0.44 ± 0.04
ξ	0.177 ± 0.065
n	0.77 ± 0.21
$\tilde{P}$ (erg cm^{-3})	$(2.7 \pm 0.7) \times 10^{-13}$

shown that SL clusters with the largest Einstein radii constitute a highly biased population with major axes preferentially aligned with the line of sight, thus increasing the magnitude of the lensing signal.

The axial ratio of the gas is $\eta_{\rm gas,a} \sim 0.77$–$0.86$ and $\eta_{\rm gas,b} \sim 0.79$–$0.87$, moving from the centre towards the virial radius.

The value of the virial radius is $R_{200} = 3809 \pm 254$ kpc. Note that we have used a triaxial definition of R_{200}, which refers to the major axis (roughly along the line of sight) of the triaxial DM halo (see equation 4). In order to make a comparison with a scalelength on the plane of the sky, we should multiply R_{200} by $\sim\eta_{\rm DM,a}$ (i.e. the virial radius corresponds to a scalelength of $\sim\eta_{\rm DM,a}R_{200} \approx 2240$ kpc). This also means that, given the SZ measurements out to $\sim$2200 kpc, SZ constrains the IC gas out to $\sim R_{200}$.

Another main result of our work is the estimate of the non-thermal pressure support, at a level up to $\sim$20 per cent in the outer volumes ($\sim R_{200}$).

In order to assess the importance of SZ data, we have performed the following test. We excluded the SZ data from the joint analysis, fixing $\tilde{P}$ to the pressure at the X-ray boundary and assuming the model of $n_{\rm e}$ employed by Morandi & Limousin (2012). This different modelling of $n_{\rm e}$ is needed because r_{c_2}, υ and n are very poorly constrained without the SZ data sets. We have obtained larger (10–25 per cent) errors on the final parameters than in the case where we include SZ data. From this test, it is clear how important SZ data are to remove degeneracy among the parameters, and how crucial in measuring the physical properties of the IC gas in the outskirts, which are inaccessible to X-ray and SL observations. Therefore, in the present analysis we need to jointly combine all the data sets (X-ray, SZ and lensing) to determine the desired physical parameters.

We stress that, in the internal regions, the physical properties of the cluster are overconstrained by our data (e.g. the thermal pressure is measured directly from the SZ data and also by the combination of X-ray density and spectroscopic temperature). This provides critical insight into our understanding of clusters, and critical tests of current models for the formation and evolution of galaxy clusters. Yet, in the outskirts, we mainly rely on the SZ data, because the outer volumes are not constrained by X-ray and SL observations. As a note of caution, we point out that the physical properties in the outskirts are then no longer overconstrained. While the SZ data are well described by our model, the addition of other constraints, such as weak lensing (WL) data and/or *Suzaku* X-ray data, might help us to gauge the impact of potential systematics on the desired properties in the outer volumes.

Fig. 3 presents the joint probability distribution among different parameters in our triaxial model. For example, we point out that there is a positive correlation between ξ and $\eta_{\rm DM,a}$ (i.e. the X-ray/lensing mass discrepancy in clusters with prominent SL features can be explained by a combination of both triaxiality and non-thermal support). We have also tried to gauge the impact of possible systematics on the inferred physical parameters. For example, the choice of using the dPIE mass distribution for lensing-only data (which constrains the two-dimensional mass out to $\sim$300 kpc) might affect, in principle, the derived parameters (e.g. the non-thermal component, which is constrained by the data out to $\sim R_{200}$). In order to test this assumption, we have also fitted the lensing-only data with a gNFW model, and we have found a projected mass profile that is consistent with that derived from a dPIE mass distribution within a few per cent. Actually, the small range constrained by the SL data does not allow us to discriminate between a dPIE and a gNFW profile. This means that the actual systematic uncertainty on the physical parameters does not depend on the assumed model of DM for lensing-only data (dPIE or gNFW), but mostly stems from the calibration uncertainties of X-ray and SZ data. For X-ray and Bolocam SZ data, the calibration uncertainties have been estimated at $\sim$6 per cent (Reese et al. 2010) and $\sim$5 per cent (Sayers et al. 2011, 2012), respectively. We repeated the MCMC analysis including the previous systematics in the X-ray and SZ data (assuming that they have Gaussian distributions) and we found that the errors on the inferred parameters become slightly larger ($\sim$10–20 per cent).

Finally, we have also compared the azimuthal angle $\tilde{\phi} = 76.4 \pm 4.7$ deg and the eccentricity on the plane of the sky ($e = 0.16 \pm 0.03$), with the values on the total two-dimensional mass from the analysis of LENSTOOL ($\tilde{\phi} = 77.4 \pm 0.6$ deg and $e = 0.11 \pm 0.02$). Note the good agreement. For the method to recover e and $\tilde{\phi}$, we refer the reader to Morandi et al. (2010).

6.2 Implications for the viability of the CDM scenario

Clusters are an optimal place to test the predictions of cosmological simulations regarding the mass profile of DM haloes. A key prediction arising from simulations of cosmic structure formation in a hierarchical, DM-dominated universe is that the density profile of DM haloes is universal across a wide range of mass scales, from dwarf galaxies to clusters of galaxies (Navarro, Frenk & White 1997). Within a scale radius, $R_{\rm s}$, the DM density asymptotes to a shallow power-law trend, $\rho_{\rm DM}(R) \propto R^{-\gamma}$, with $\gamma = 1$, steepening at increasing radii. Simulations also suggest that galaxy cluster concentrations, which are a measure of a halo's central density, decrease gradually with virial mass. Nevertheless, the value of the logarithmic inner slope γ and the actual mass–concentration relation are still debated.

Recently, in investigations of the mass distributions of individual galaxy clusters, high concentration parameters, very large Einstein radii and high efficiency in generating giant arcs have been measured. Thus, there is a major inconsistency with the theoretical CDM expectations (Broadhurst et al. 2005; Limousin et al. 2007a; Zitrin et al. 2011).

Moreover, measurements of γ over various mass scales have proved to be controversial, yielding conflicting values of γ, with large scatter from one cluster to another. Shallow cusps have been inferred by the analysis of Sand et al. (2008), raising doubts on the predictions of the CDM scenario. However, these determinations rely on the standard spherical modelling of galaxy clusters.

The disagreement between theory and observation can be explained by triaxiality. In clusters that are elongated along the line of sight, the measured concentration parameter is substantially biased up with respect to the theoretical expectations, and the observed lensing properties are boosted (Meneghetti et al. 2010b). Moreover, elongation/flattening of the sources along the line of sight, as well as the degeneracy of γ with other parameters (i.e. the concentration parameter and the scale radius) likely affect the estimated values of γ. Therefore, knowledge of the intrinsic shape and orientation of haloes is crucial for unbiased determinations of the inner slope of the DM and concentration parameter, and hence for the assessment of the viability of the standard cosmological framework (Morandi et al. 2010).

One of the main results of the work presented here is a measurement of the central slope of the DM $\gamma = 1.01 \pm 0.06$ using a triaxial joint analysis for Abell 1835. This value agrees with the CDM predictions from Navarro et al. (1997) (i.e. $\gamma = 1$). We point out that we have removed the central 25 kpc in the lensing data, to

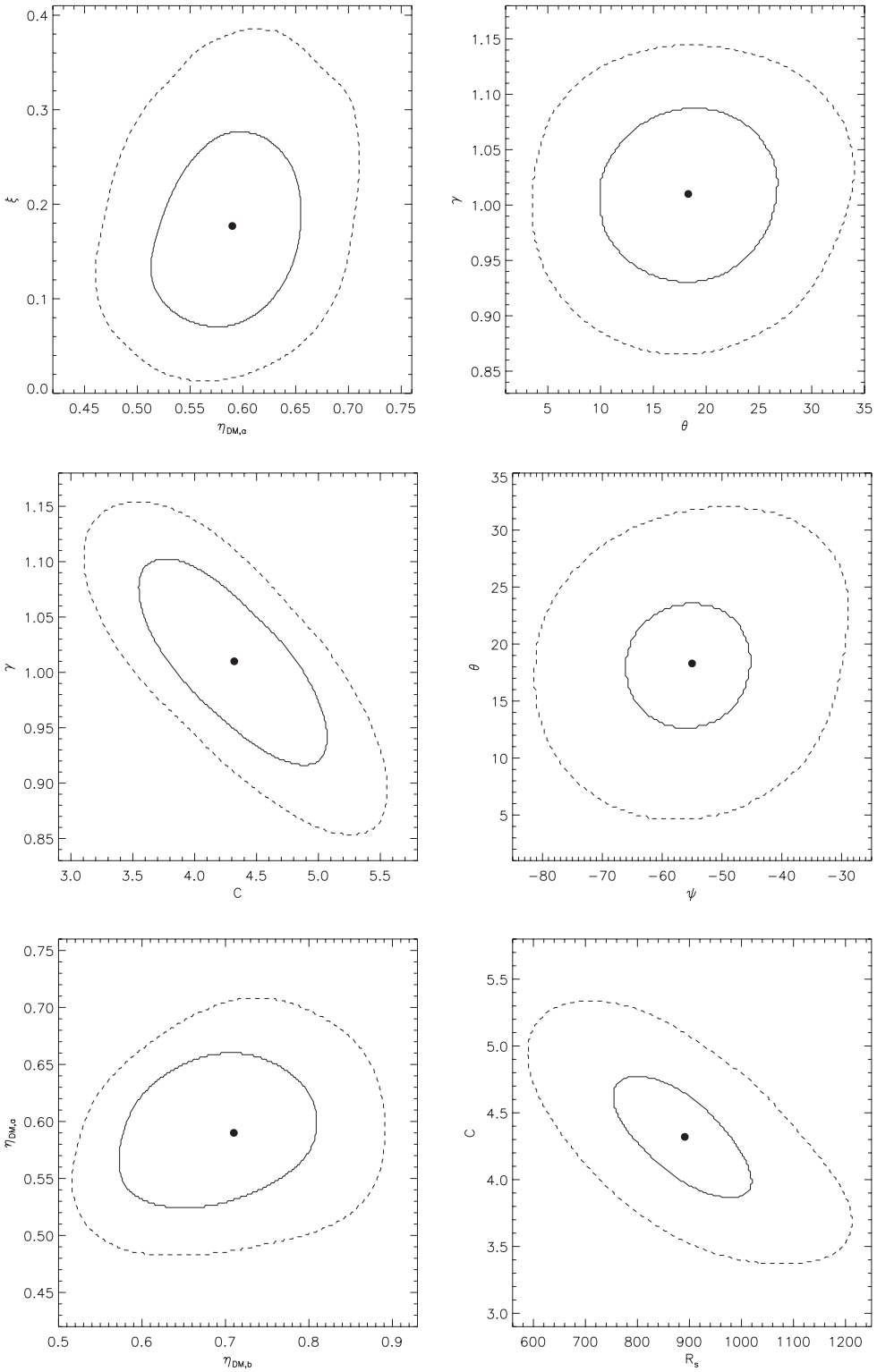

Figure 3. Marginal probability distribution among different parameters in our triaxial model. The solid and dashed lines represent the 1σ and 2σ error regions, respectively, while the dots represent the expectation values.

avoid contamination from the cD galaxy, although we have checked that there is very little dependence of the physical parameters in the radius of the masked region. The value of the concentration parameter $C = 4.32 \pm 0.44$ is in agreement with the theoretical expectation from *N*-body simulations of Neto et al. (2007) and Duffy et al. (2008), where $C \sim 4$ at the redshift and for the virial mass of Abell 1835, and with an intrinsic scatter of ∼20 per cent. Using a lensing-only analysis assuming spherical geometry, we infer a large value of the concentration parameter $C = 6.19 \pm 0.63$. This is above the standard *C*–*M* relation, and it conflicts with the predictions of

the standard model. This confirms our insights about the role of the effects of geometry on the cluster concentrations.

Given that numerical simulations customarily retrieve the concentration parameter by using a spherically averaged total density profile, we wonder whether a comparison of such simulations with the concentration parameter inferred in our triaxial framework is tenable. Thus, we have generated an ideal ellipsoidal NFW cluster with the parameters fixed to those of Abell 1835 (we fixed $\gamma = 1$ for simplicity in the comparison with simulations). Then, we measured C by spherically averaging the total density profile. We have found that such a concentration parameter is slightly lower ($\sim$4 per cent) than the value in the triaxial framework. Given that this bias is much smaller than the intrinsic scatter of C in numerical simulations ($\sim$20 per cent; see Neto et al. 2007), we conclude that a comparison of our findings with simulations is still convincing.

Also, we report the value of the concentration parameter for an X-ray-only analysis under the assumption of spherical geometry, $C = 4.40 \pm 0.23$.

Morandi et al. (2010, 2011a,b) and Morandi & Limousin (2012) have analysed the galaxy clusters Abell 1689, Abell 383 and MACS J1423.8+2404 in our triaxial framework. We have found that γ and C are close to the CDM predictions for these clusters, in agreement with the results in the present paper. Our findings provide further evidence that supports the CDM scenario.

We also find that our inferred value of the concentration parameter and the axial ratios agree very well with those of Corless et al. (2009), who constrained the triaxial shape of the total mass distribution of Abell 1835 using weak lensing data and under a range of Bayesian priors derived from theory.

6.3 Non-thermal gas pressure

Hydrodynamical simulations have shown that a significant fraction of the total energy of the IC gas is non-thermal, mainly because of random gas motions and turbulence in the same IC gas. This energy is sourced by several mechanisms: plasma instabilities, mergers and subcluster assembly in the hierarchical structure formation scenario, shock waves, wakes of galaxies moving into the IGM, outflows from active galactic nuclei (AGNs) hosted in the centre of galaxy clusters and galactic winds (Norman & Bryan 1999). In particular, in the hierarchical structure formation scenario, turbulent motions should occur in the IC gas while the matter continues to accrete along filaments. Indeed, gas accreting on to clusters of galaxies has bulk velocities of about $v = 1900(T/6.7)^{0.52}$ km s^{-1} at 1 Mpc (see Miniati et al. 2000). Here, T is the gas temperature. This velocity is comparable to the expected sound speed of 1000–1500 km s^{-1} of the ICM, and hence it generates turbulent gas motions at the boundary between the bulk flow and the thermalized ICM (Vazza et al. 2009). This non-hydrostatic energy should then cascade from large to small scales and it can eventually dissipate into the gas, leading to a (partial) thermalization of the IC gas. Yet, the total energy budget – in the form of turbulent motions inside galaxy clusters, as well as their distribution and their connection with cluster dynamics and the non-gravitational process in galaxy clusters – is still open to debate in the literature.

While the level of non-thermal pressure is typically found to be small in the central regions of clusters, it increases with radius, becoming a significant fraction of the total pressure in the outer volumes (Lau et al. 2009). It is also clear that non-thermal pressure support causes a systematic underestimate of the cluster mass recovered under the assumption of strict HE (Nagai et al. 2007; Meneghetti et al. 2010a). This translates into biases in the determination of the cosmological parameters.

Some observational evidence of non-thermal pressure has also been published in the last few years. Schuecker et al. (2004) obtained spatially resolved gas pressure maps of the Coma cluster, which indicated the presence of a significant amount of turbulence, with a spectrum of the fluctuations consistent with Kolmogorov turbulence. This yielded a lower limit of $\sim$10 per cent of the total IC gas pressure in turbulent form. Additional evidence of turbulent motions inside nearby galaxies comes from the observations of pressure fluctuations in Abell 754 (Henry, Finoguenov & Briel 2004) and Perseus (Fabian et al. 2003). The observational results of Mahdavi et al. (2008), based on X-ray and WL mass determinations, indicate that there is a radial trend of the X-ray/WL mass ratio, which is interpreted as caused by non-thermality increasing towards the outer regions. Nevertheless, their findings hinge on the assumed spherical geometry, so they have not disentangled the effect of triaxiality from non-thermal pressure support. Morandi & Limousin (2012) measured the non-thermal component of the gas ($\sim$10 per cent) relative to the total energy budget of the inner volumes of the IC gas of Abell 383.

Motivated by the need to study the magnitude and gradient of the non-thermal pressure support, and given the constraints on the IC gas provided by SZ data out to $\sim R_{200}$, here we have implemented a model where $P_{\rm nt}$ is the fraction of the total pressure $P_{\rm tot}$. We set this fraction to be a power law with the radius. The theoretical work of Shaw et al. (2010), based on 16 simulated clusters, has shown that this model reasonably reproduces the trend of $P_{\rm nt}/P_{\rm tot}$ throughout a cluster. They found a slope of 0.8 ± 0.25, in agreement with our measured value, and a normalization[3] $\gtrsim$0.3, in marginal ($\sim 2\sigma$) disagreement with our analysis, where we have found a normalization $\xi = 0.177 \pm 0.065$. Therefore, our findings indicate that the level of turbulence in the numerical simulations might be overestimated.

We stress that this is the first observational measurement of the non-thermal pressure out to R_{200}, recovered using a triaxial joint X-ray, SZ and lensing analysis. Thus, our results can provide an anchor for the numerical models of ICM physics and for simulations of the formation and ongoing growth of galaxy clusters, given that measurements of the non-thermal energy in the IC gas are a proxy of the amount of energy injected into clusters from mergers, hierarchical assembly of substructures, accretion of material or feedback from AGNs. In this perspective, the cooling–pre-heating simulations of Stanek et al. (2010) suggest that the IC gas in the gravitation-only simulations develops more substructures with time than in the former. The suppression of substructures caused by the pre-heating leads to a lower level of kinetic energy in bulk motions with respect to simulations without pre-heating, confirming that the level of non-thermal pressure is sensitive to the particulars of the physical processes. Therefore, a more extensive physical treatment, which incorporates further physical processes in the ICM that are currently uncertain [e.g. galaxy and supermassive black hole formation, magnetohydrodynamics, viscosity, conduction, star formation feedback, magnetic fields and non-thermal plasmas, and (pre)-heating], might be needed (or improved) in simulations in order to match the amount of non-thermal energy with our observational findings.

Moreover, given that hydrodynamical simulations indicate that the non-thermal pressure provided by gas motions significantly

[3] Note that in Shaw et al. (2010) the scale radius for $P_{\rm nt}$ refers to R_{500}, so we have renormalized their results to R_{200}.

modifies the ICM profiles in the cluster outskirts (Lau et al. 2009), the non-thermal pressure must be accurately determined in order to obtain unbiased measurements of the physical parameters.

As a note of caution, we remind the reader that our results were obtained for just one galaxy cluster, although it is expected that the observed physical processes are common, at least for relaxed objects. Thus, we plan to collect data for a larger sample of clusters to strengthen the statistical significance of our findings.

We also report on the work of Sanders et al. (2010), who placed a direct limit on turbulence based on the non-thermal velocity broadening measured from the emission lines originating in the central 30 kpc of Abell 1835. They have found that the ratio of turbulent to thermal energy density in the core is less than 13 per cent, in agreement with our present work.

6.4 Physical properties in the outskirts

The outskirts of galaxy clusters present an opportunity to study the formation of large-scale structure as it happens. They have special importance in cluster cosmology, because they are believed to be much less prone to complicated cluster astrophysics, such as radiative gas cooling, star formation and energy injection from AGNs, although they are potentially more susceptible to the turbulence and bulk flows that result from structure formation processes (Section 6.3). The physics of the IC gas in the outer volumes is relatively simple and nearly self-similar, being dominated by the gravity-driven collisionless dynamics of DM and hydrodynamics of the gas. However, until very recently, observational studies of the ICM have been limited to radii that are considerably smaller than the virial radius of clusters. Here, we aim to further the understanding of the properties of the ICM in the outskirts of Abell 1835, by comparing our findings with the results of hydrodynamical numerical simulations.

Our spherically averaged gas density has good agreement with the predictions from hydrodynamical numerical simulations, including cooling, star formation and supernovae feedback (Roncarelli et al. 2006), although with a slightly flatter slope. A possible explanation for this trend is that in the above-mentioned simulation Roncarelli et al. did not include AGN feedback and/or pre-heating, which might be important, even at large radii, for smoothing the accretion pattern and leading to a flatter gas distribution (Borgani et al. 2005).

It is interesting to point out that some recent *Suzaku* observations have indicated shallow density/entropy profiles in cluster outskirts, at variance with the results from previous *ROSAT* observations (Vikhlinin, Forman & Jones 1999; Eckert et al. 2012), and with the results from numerical simulations (Roncarelli et al. 2006). Thus, the behaviour of the gas density in cluster outskirts is still the subject of debate. In this context, Simionescu et al. (2011) and George et al. (2009) have analysed *Suzaku* X-ray observations along narrow arms, and they have found that the electron density decreases steadily with radius, approximately following a power-law model. On the contrary, we observe a general trend of steepening in the radial profiles of the gas density beyond $0.2\,R_{200}$, with a logarithmic slope of $\sim$2–2.3 in the range (0.3–1) R_{200}. Eckert et al. (2012) have performed a stacking of the density profiles of a sample of clusters observed through *ROSAT* in order to analyse the outskirts of clusters, although they have not been able to determine any spectral information (i.e. the gas temperature) from these data. Their average density profile steepens beyond R_{500}, in agreement with the present work and with previous works by *ROSAT* (Vikhlinin et al. 1999). Eckert et al. (2012) have also argued that the shallow density profiles observed in some clusters by *Suzaku* might be induced by observations in preferential directions (e.g. along filaments) and that they do not reflect the typical behaviour of the outer regions of clusters.

It is also interesting to observe that the normalization of the average density near the virial radius from Eckert et al. (2012) is about 50 per cent higher than in the present analysis, where we have found a very good agreement with the predictions from the simulations of Roncarelli et al. (2006). Unlike SZ data, X-ray brightness is biased by dense, cold clumps in the outer volumes, as it is traced by the square of the gas density, therefore boosting the same gas density.

We also observe a good agreement of our slope of the temperature with the theoretical predictions of Roncarelli et al. (2006) out to $0.7\,R_{200}$, although near R_{200} our temperature profile is steeper, which suggests the presence of cold, clumpy gas.

Now we focus on the entropy profile $S = kT/n_{\rm e}^{2/3}$, because this is a powerful tool to trace the thermal history of the ICM. Indeed, the gas entropy records the thermodynamic history of the ICM as the product of both gravitational and non-gravitational processes, shaping its observed structure accordingly (Voit 2005). The measurements of the gas entropy in the inner regions ($0.1\,R_{200}$) show that the observed value of S is higher than that expected from the adiabatic scenario (Ponman, Cannon & Navarro 1999), which includes only gravity. This excess in the entropy (labelled entropy 'floor' or 'ramp'), with respect to the prediction of the adiabatic model, calls for some energetic mechanism, in addition to gravity, such as (pre)-heating and cooling (Bryan 2000; Borgani et al. 2005; Morandi & Ettori 2007). Somehow, these non-gravitational processes intervene to break the expected self-similarity of the IC gas in the innermost regions. Nevertheless, in the outer volumes, simple theoretical models predict that the entropy S should be self-similar and that it should behave as a power law with radius. Models of shock-dominated spherical collapse show that matter is shock-heated as it falls into clusters under the pull of gravity, with a slope of $\sim$1.1 (Tozzi & Norman 2001). In this paper, we aim to compare the theoretical predictions with the observed entropy profile out to R_{200}.

It is interesting to point out that our entropy profile (see Fig. 4) roughly follows this expected trend for $0.2\,R_{200} \lesssim R \lesssim 0.8\,R_{200}$ with a logarithmic slope of $\sim$1. In particular, in this spatial range, we find good agreement with the adiabatic predictions of Voit et al. (2005) by considering smoothed particle hydrodynamics (SPH) simulations through the GADGET code (Springel, Yoshida & White 2001; Springel & Hernquist 2002), where the entropy is defined as

$$S(R) = S_{200}\,1.32(R/R_{200})^{1.1}. \quad (18)$$

Here, S_{200} is a characteristic value of the entropy at the overdensity of 200 (see, for example, equation 2 in Voit et al. 2005). Voit et al. also consider semi-analytical models by using clusters simulated by the AMR code ENZO (Norman & Bryan 1999; O'Shea et al. 2005). In this case, the normalization of the above theoretical relation is $\sim$10 per cent higher than in the SPH simulations, in better agreement with our constraints. This suggests that for $R \gtrsim 0.2\,R_{200}$, the physics of the X-ray emitting gas is relatively simple and nearly self-similar, and SZ measurements can be used robustly for cosmological works.

Nevertheless, we observe a flattening of S from the power-law shape in the outskirts ($R \gtrsim 0.8\,R_{200}$), as inferred from *Suzaku* X-ray observations (George et al. 2009; Simionescu et al. 2011). This is perhaps indicative of infalling gas, which is not dynamically stable (Nagai & Lau 2011). While numerical simulations predict gas clumping in the cluster outskirts, SZ data are less biased by dense, cold clumps and gas in a multiphase state in the outer volumes with respect to X-ray data, because the SZ intensity depends linearly

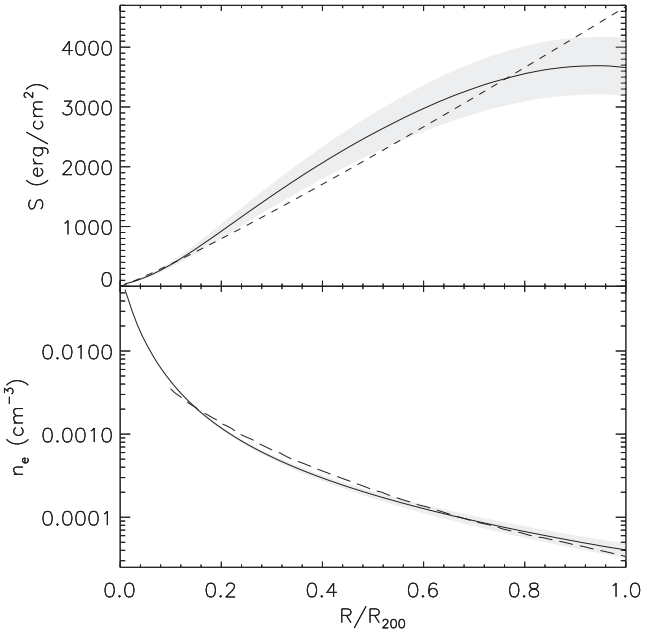

Figure 4. Top panel: spherically averaged entropy profiles S for Abell 1835 recovered using triaxial joint X-ray, SZ and lensing analyses. The solid line represents the expectation value for S, while the 1σ errors are represented by the grey shaded region. The dashed line represents the predictions of Voit, Kay & Bryan (2005), where the entropy is defined as $S(R) = S_{200}\,1.32(R/R_{200})^{1.1}$. Here, S_{200} is a characteristic value of the entropy at an overdensity of 200 (see, for example, equation 2 in Voit et al. 2005). Lower panel: spherically averaged gas density profile n_e for Abell 1835. The solid line represents the expectation value for n_e, while the 1σ errors are represented by the grey shaded region. The long-dashed line represents the predictions from Roncarelli et al. (2006).

on the density, unlike the X-ray flux. Indeed, unlike the present analysis, previous *Suzaku* X-ray measurements point to a more pronounced flattening of S in the outer regions.

The gentle flattening of the entropy profile in the outskirts suggests the need for a cool phase gas and non-thermal pressure support in order to maintain dynamic stability, as already deduced in Section 6.3. Afshordi et al. (2007) stacked *WMAP* observations of a large sample of massive clusters and found a deficit in the thermal energy in the outskirts from the SZ profile, also arguing for a cool phase of the ICM. Yet, it is not understood how these different phases would mix, and complicated gas physics are likely to result, as suggested from the marginal disagreement in the level of non-thermal pressure between simulations and the current work.

7 SUMMARY AND CONCLUSIONS

In this paper, we have employed a physical cluster model for Abell 1835 with a triaxial mass distribution including support from non-thermal pressure, proving that it is consistent with all the X-ray, SZ and lensing observations and the predictions of CDM models. This model relies on the following assumptions: (i) the use of a dPIE mass model for the lensing data; (ii) an assumption of generalized HE, which also accounts for the non-thermal energy contribution; (iii) the non-thermal contribution traces the thermal pressure up to a scale factor taken to be a power law with the cluster radius; (iv) the DM halo density that follows a gNFW triaxial model. We stress that, given the complementary data sets that have been included in this work, we do not need to rely on any prior from numerical simulations.

We have presented the first observational measurement of the non-thermal pressure out to R_{200}. The level of non-thermal pressure has been evaluated to be a few per cent of the total energy budget in the internal regions, while it reaches about 20 per cent in the outer volumes, a value that is lower than the predictions from numerical simulations. This indicates that an improved physical treatment in the ICM might be needed in simulations to match the amount of non-thermal energy with our observational findings. This has important consequences for estimating the amount of energy injected into clusters from mergers, the accretion of material or feedback from AGNs.

We have analysed the physical properties of the IC gas in the outer volumes out to R_{200}, focusing on the entropy, which is a powerful tool for tracing the thermal history of the IC gas. We have found good agreement with the theoretical predictions, indicating that outside the innermost regions the physics of the X-ray emitting gas is relatively simple and nearly self-similar. Nevertheless, we observe that entropy tends to gently flatten in the outer volumes, which is likely to indicate infalling clumpy and cold gas that is not dynamically stable. In this context, SZ data are crucial for unbiased measurements of the cluster physical properties out to large radii, such as those presented here.

ACKNOWLEDGMENTS

AM acknowledges support from the Israel Science Foundation grant 823/09. ML acknowledges the Centre National de la Recherche Scientifique (CNRS) for its support. The Dark Cosmology Centre is funded by the Danish National Research Foundation. This work has been conducted using facilities offered by the Centre de Données Astrophysique de Marseille (CeSAM; http://lam.oamp.fr/cesam/). JS was partially supported by a NASA Graduate Student Research Fellowship and a NASA Postdoctoral Programme fellowship (NSF/AST-0838261 and NASA/NNX11AB07G). NC was partially supported by a NASA Graduate Student Research Fellowship. Bolocam observations and analyses were also supported by the Gordon and Betty Moore Foundation. Bolocam was constructed and commissioned using funds from NSF/AST-9618798, NSF/AST-0098737, NSF/AST-9980846, NSF/AST-0229008 and NSF/AST-0206158. SA and EP were partially supported by the National Science Foundation grant AST-0649899. SA was partially supported by a postdoctoral fellowship and travel grants from the University of Southern California (USC) Women in Science and Engineering (WiSE) programme, and EP was partially supported by a NASA grant NNXO7AH59G and JPL-*Planck* subcontract 1290790. The spectroscopic optical data are based on observations collected at the European Southern Observatory, Chile.

REFERENCES

Afshordi N., Lin Y.-T., Nagai D., Sanderson A. J. R., 2007, MNRAS, 378, 293

Ameglio S., Borgani S., Pierpaoli E., Dolag K., Ettori S., Morandi A., 2009, MNRAS, 394, 479

Arnaud K. A., 1996, in Jacoby G. H., Barnes J., eds, ASP Conf. Ser. Vol. 101, Astronomical Data Analysis Software and Systems V. Astron. Soc. Pac., San Francisco, p. 17

Arnaud M., Pratt G. W., Piffaretti R., Böhringer H., Croston J. H., Pointecouteau E., 2010, A&A, 517, A92

Borgani S., Finoguenov A., Kay S. T., Ponman T. J., Springel V., Tozzi P., Voit G. M., 2005, MNRAS, 361, 233

Broadhurst T. et al., 2005, ApJ, 621, 53
Bryan G. L., 2000, ApJ, 544, L1
Corless V. L., King L. J., Clowe D., 2009, MNRAS, 393, 1235
Duffy A. R., Schaye J., Kay S. T., Dalla Vecchia C., 2008, MNRAS, 390, L64
Eckert D. et al., 2012, A&A, 541, A57
Elíasdóttir Á. et al., 2007, preprint (arXiv:0710.5636)
Ettori S., Morandi A., Tozzi P., Balestra I., Borgani S., Rosati P., Lovisari L., Terenziani F., 2009, A&A, 501, 61
Fabian A. C., Sanders J. S., Allen S. W., Crawford C. S., Iwasawa K., Johnstone R. M., Schmidt R. W., Taylor G. B., 2003, MNRAS, 344, L43
Gehrels N., 1986, ApJ, 303, 336
Gelman A., Rubin D. B., 1992, Stat. Sci., 7, 457
George M. R., Fabian A. C., Sanders J. S., Young A. J., Russell H. R., 2009, MNRAS, 395, 657
Henry J. P., Finoguenov A., Briel U. G., 2004, ApJ, 615, 181
Itoh N., Kohyama Y., Nozawa S., 1998, ApJ, 502, 7
Jing Y. P., Suto Y., 2002, ApJ, 574, 538
Jullo E., Kneib J.-P., Limousin M., Elíasdóttir Á., Marshall P. J., Verdugo T., 2007, New J. Phys., 9, 447
Kaastra J. S., 1992, An X-Ray Spectral Code for Optically Thin Plasmas (Internal SRON-Leiden Report, updated version 2.0)
Lau E. T., Kravtsov A. V., Nagai D., 2009, ApJ, 705, 1129
Lee J., Suto Y., 2003, ApJ, 585, 151
Lee J., Suto Y., 2004, ApJ, 601, 599
Liedahl D. A., Osterheld A. L., Goldstein W. H., 1995, ApJ, 438, L115
Limousin M., Kneib J.-P., Natarajan P., 2005, MNRAS, 356, 309
Limousin M. et al., 2007a, ApJ, 668, 643
Limousin M., Kneib J. P., Bardeau S., Natarajan P., Czoske O., Smail I., Ebeling H., Smith G. P., 2007b, A&A, 461, 881
Limousin M. et al., 2008, A&A, 489, 23
Limousin M., Sommer-Larsen J., Natarajan P., Milvang-Jensen B., 2009, ApJ, 696, 1771
Mahdavi A., Chang W., 2011, ApJ, 735, L4
Mahdavi A., Hoekstra H., Babul A., Henry J. P., 2008, MNRAS, 384, 1567
Mantz A., Allen S. W., Rapetti D., Ebeling H., 2010, MNRAS, 406, 1759
Mazzotta P., Rasia E., Moscardini L., Tormen G., 2004, MNRAS, 354, 10
Meneghetti M., Rasia E., Merten J., Bellagamba F., Ettori S., Mazzotta P., Dolag K., Marri S., 2010a, A&A, 514, A93
Meneghetti M., Fedeli C., Pace F., Gottlöber S., Yepes G., 2010b, A&A, 519, A90
Miniati F., Ryu D., Kang H., Jones T. W., Cen R., Ostriker J. P., 2000, ApJ, 542, 608
Miralda Escude J., Babul A., 1995, ApJ, 449, 18
Morandi A., Ettori S., 2007, MNRAS, 380, 1521
Morandi A., Limousin M., 2012, MNRAS, 421, 3147
Morandi A., Ettori S., Moscardini L., 2007, MNRAS, 379, 518
Morandi A., Pedersen K., Limousin M., 2010, ApJ, 713, 491
Morandi A., Pedersen K., Limousin M., 2011a, ApJ, 729, 37
Morandi A., Limousin M., Rephaeli Y., Umetsu K., Barkana R., Broadhurst T., Dahle H., 2011b, MNRAS, 416, 2567
Nagai D., Lau E. T., 2011, ApJ, 731, L10
Nagai D., Kravtsov A. V., Vikhlinin A., 2007, ApJ, 668, 1
Natarajan P., Kneib J.-P., Smail I., Treu T., Ellis R., Moran S., Limousin M., Czoske O., 2009, ApJ, 693, 970
Navarro J. F., Frenk C. S., White S. D. M., 1996, ApJ, 462, 563
Navarro J. F., Frenk C. S., White S. D. M., 1997, ApJ, 490, 493
Neto A. F. et al., 2007, MNRAS, 381, 1450
Newman A. B., Treu T., Ellis R. S., Sand D. J., 2011, ApJ, 728, L39
Norman M. L., Bryan G. L., 1999, in Miyama S. M., Tomisaka K., Hanawa T., eds, Astrophys. Space Sci. Libr. Vol. 240, Numerical Astrophysics. Kluwer, Dordrecht, p. 19
Oguri M., Blandford R. D., 2009, MNRAS, 392, 930
Oguri M., Takada M., Umetsu K., Broadhurst T., 2005, ApJ, 632, 841
O'Shea B. W., Bryan G., Bordner J., Norman M. L., Abel T., Harkness R., Kritsuk A., 2005, in Plewa T., Linde T., Weirs V. G., eds, Lecture Notes in Computational Science and Engineering Vol. 41, Adaptive Mesh Refinement – Theory and Applications. Springer, Berlin, p. 341
Ponman T. J., Cannon D. B., Navarro J. F., 1999, Nat, 397, 135
Reese E. D., Kawahara H., Kitayama T., Ota N., Sasaki S., Suto Y., 2010, ApJ, 721, 653
Richard J. et al., 2010, MNRAS, 404, 325
Roncarelli M., Ettori S., Dolag K., Moscardini L., Borgani S., Murante G., 2006, MNRAS, 373, 1339
Sand D. J., Treu T., Ellis R. S., Smith G. P., Kneib J., 2008, ApJ, 674, 711
Sanders J. S., Fabian A. C., Smith R. K., Peterson J. R., 2010, MNRAS, 402, L11
Sanders J. S., Fabian A. C., Smith R. K., 2011, MNRAS, 410, 1797
Sarazin C. L., 1988, J. British Astron. Assoc., 98, 212
Sayers J., Golwala S. R., Ameglio S., Pierpaoli E., 2011, ApJ, 728, 39
Sayers J., Czakon N. G., Golwala S. R., 2012, ApJ, 744, 169
Schuecker P., Finoguenov A., Miniati F., Böhringer H., Briel U. G., 2004, A&A, 426, 387
Shaw L. D., Weller J., Ostriker J. P., Bode P., 2006, ApJ, 646, 815
Shaw L. D., Nagai D., Bhattacharya S., Lau E. T., 2010, ApJ, 725, 1452
Simionescu A. et al., 2011, Sci, 331, 1576
Springel V., Hernquist L., 2002, MNRAS, 333, 649
Springel V., Yoshida N., White S. D. M., 2001, New Astron., 6, 79
Stanek R., Rasia E., Evrard A. E., Pearce F., Gazzola L., 2010, ApJ, 715, 1508
Sunyaev R. A., Zel'dovich Y. B., 1970, Comments Astrophys. Space Phys., 2, 66
Tozzi P., Norman C., 2001, ApJ, 546, 63
Vazza F., Brunetti G., Kritsuk A., Wagner R., Gheller C., Norman M., 2009, A&A, 504, 33
Vikhlinin A., Forman W., Jones C., 1999, ApJ, 525, 47
Voit G. M., 2005, Rev. Mod. Phys., 77, 207
Voit G. M., Kay S. T., Bryan G. L., 2005, MNRAS, 364, 909
Wang J., White S. D. M., 2009, MNRAS, 396, 709
Wetzel A. R., White M., 2010, MNRAS, 403, 1072
Wyithe J. S. B., Turner E. L., Spergel D. N., 2001, ApJ, 555, 504
Zitrin A., Broadhurst T., Barkana R., Rephaeli Y., Benítez N., 2011, MNRAS, 410, 1939

This paper has been typeset from a TEX/LATEX file prepared by the author.